processes

MDPI

Article

Analysis of Crushing Performance of Toothed Double-Roll Crusher for Coal Particle Based on Discrete Element Method

Zeren Chen [1], Guoqiang Wang [2], Zhengjie Lei [3], Duomei Xue [4,*] and Zhengbin Liu [2,*]

[1] College of Mechanical Engineering, Taiyuan University of Technology, Taiyuan 030024, China; chenzeren@tyut.edu.cn
[2] School of Mechanical and Aerospace Engineering, Jilin University, Changchun 130025, China; wangguoqiang0228@163.com
[3] Taiyuan Heavy Industry Co., Ltd., Taiyuan 030032, China; czrndy@163.com
[4] College of Chemical Engineering and Technology, Taiyuan University of Science and Technology, Taiyuan 030024, China
* Correspondence: xueduomei@tyust.edu.cn (D.X.); zbliu23@mails.jlu.edu.cn (Z.L.); Tel.: +86-18844076593 (D.X.)

Abstract: The large toothed double-roll crusher, as key crushing equipment for open pit mines, is very necessary to analyse its crushing performance at different feed particle sizes, compressive strengths of coal, and rotation speeds of toothed rollers. Firstly, a toothed double-roll crusher is taken as the research object in this paper; the coupling simulation model of the toothed double-roll crusher based on the DEM-MBD and Ab-T_{10} breakage model is constructed. The validity of the coupling simulation model is verified through the actual measurement data. On this basis, the crushing performance under variable factors is analysed by integrating comprehensive tests. The results show that the rotation speed of the toothed roller is the main influence factor on the crushing performance of the toothed double-roll crusher when it works at 25~33.3 r/min. With the increase in compressive strength of coal, the productivity decreases, and this phenomenon disappears gradually at 33.3~42 r/min. Further, a 5–20% increase in the large size of the coal particles can improve 10% crushing quality with a discharge size lower than 300 mm and approximately 25% productivity of the toothed double-roll crusher. Finally, the power density is reduced as the mass percentage of large-sized coal particles increases, and this phenomenon is weakened with the increase in the compressive strength of coal.

Keywords: toothed double-roll crusher; discrete element method; Ab-T_{10}; crushing performance; power density; variables analysis

check for updates

Academic Editor: Alberto Di Renzo

Received: 28 January 2025
Revised: 16 February 2025
Accepted: 19 February 2025
Published: 21 February 2025

Citation: Chen, Z.; Wang, G.; Lei, Z.; Xue, D.; Liu, Z. Analysis of Crushing Performance of Toothed Double-Roll Crusher for Coal Particle Based on Discrete Element Method. *Processes* **2025**, *13*, 613. https://doi.org/10.3390/pr13030613

Copyright: © 2025 by the authors. Licensee MDPI, Basel, Switzerland. This article is an open access article distributed under the terms and conditions of the Creative Commons Attribution (CC BY) license (https://creativecommons.org/licenses/by/4.0/).

1. Introduction

As the core equipment of large-scale mining crushing plants, the toothed double-roll crusher [1] is widely used in open-pit coal mines, such as the Heidaigou open-pit coal mine, which is the largest open-pit coal mine in China. The performance of the toothed double-roll crusher determines the productivity of the whole open-pit mine, so clarifying the crushing performance of the toothed double-roll crusher can provide a basis for its subsequent performance improvement and also help the relevant researchers to further clarify its crushing mechanism.

The toothed double-roll crusher (TDRC) is a typical multi-body system. It is used primarily to crush soft materials such as coal, limestone, and soft or sticky iron ore. It consists of a pair of oppositely rotating rolls, which have a series of intermeshing crushing

toothed rings protruding from the roll surfaces. The ore can be crushed through a combination of compression and ripping. The particle flow and breakage behaviour during the crushing process are important for the performance of TDRC. At present, there is a limited understanding of these fundamentals.

For different crushers, ore particles are crushed based on different crushing mechanisms. In compression-based crushers [2–5], the ore materials could be broken into coarse particles mainly resulting from the induced tensile failure and fines mainly from the compressive failure near the points of loading. There are internal stresses in the particles broken by the pressure that can later cause cracking. On the other hand, the ore materials in impact-based crushers [6–8] are crushed mainly by tensile failure, which causes immediate fracture with no residual stresses. Compared with the above-mentioned crushers, TDRC breaks particles by a complex combination of pressed, split, and shear forces. It should be noticed that the shear resistance of ore materials is generally much lower than the compression resistance. Thus, the ore particles can be crushed more easily as a result of the combined crushing mechanism under low crushing force, which makes the TDRC a new type of high-efficiency and energy-saving crusher [9].

At present, the research method on material crushing behaviour is mainly a fusion of computational analysis and experimental validation, which is a cost-effective and reliable way [10]. Here, computational analysis includes numerical simulation and theoretical calculations. In the case of theoretical calculations, Evertsson et al. [11] proposed an alternative flow model of the cone crusher that is better adapted for pressure and wear prediction. Huang et al. [12] developed a new multi-objective model of the crushing chamber, output, and size reduction based on equations of motion and population balance models. Wu et al. [13,14] presented a productivity calculation method for eccentric roll crushers based on the breakage model developed by Evertsson [15]. It can be seen that the theoretical calculation can effectively predict the crushing performance of the crusher, including discharge size and productivity, etc., but cannot visually reflect particle flow and breakage behaviour of the material inside the crusher, which is the advantage of numerical simulation.

As far as numerical simulation is concerned, the discrete element method (DEM) has become an important tool for understanding the comminution fundamentals of comminution devices. The scale and complexity of its applications in modelling crushing and equipment wear have increased [16,17], where physical reproduction of ore particle crushing is mainly achieved by the bonded particle model (BPM) [18,19] and the Ab-T_{10} breakage model [20,21]. Wu et al. [14] simulated the dynamic characteristics of the C900 cone crusher by using the bonded particle model and the particle replacement method. Quist et al. [22,23] conducted a crushing characteristics and performance evaluation of iron ore in a cone crusher based on the same methodology. Li et al. [24] developed a DEM model of the crushing process of a toothed double-roll crusher using the BPM. Although BPM can characterise the particle crushing process, it cannot accurately characterise the shape and size distribution of the crushed particles. Cui et al. [1] proposed a novel reliability design method for the planetary gear of TDRC by using BPM. Because of the problems that the current solid organic fertiliser is easy to agglomerate in the fermentation and stacking process, the fertiliser efficiency is brutal to release, and the strip application is difficult to discharge, Wang et al. [25] proposed a solid organic fertiliser crushing strip application method combining propeller blades and differential speed rollers based on BPM. Our team has previously made a series of advances in analysing the performance of a series of gyratory crushers based on BPM [3,4]. However, constructing a complex ore particle population model is a key problem that is difficult to solve, which is achievable by the Ab-T_{10} breakage model rather than the BPM. The ore particles constructed based on

BPM are mainly spherical particles after crushing, which is quite different from the actual polyhedral-shaped ore particles. Currently, the Ab-T_{10} breakage model is mainly used for particle breakage analysis in chemical processes, and very limited relevant reports have been seen in TDRC [26].

Therefore, the TDRC used in the Heidaigou open-cast coal mine is taken as the specific analysis object in this paper. Its performances, including productivity, crushing force, particle size distribution, power consumption, and power density, are explored by DEM-MBD (multi-body dynamics) and the Ab-T_{10} breakage model. Further, the influence of the feed size, compressive strengths of materials, and rotation speed of the toothed roller on the TDRC performances is analysed by integrating comprehensive tests.

2. Materials and Methods

2.1. Toothed Double-Roll Crusher

The TDRC of the mining crushing plant is mainly used for the primary crushing of ore materials, as shown in Figure 1. It mainly consists of a feeding bin feeding material, a reducer (with a motor) providing rotation force, a shattering beam for secondary crushing, a collecting bin for the collection of the crushed material, two synchromesh gears passing rotation motion, a pair of toothed rollers crushing ore materials, a crushing chamber for material crushing, and a plurality of comb teeth set in the crushing chamber. Further, the rotation speed of the toothed rollers is controlled by a variable-frequency drive connected to the motor. A feeding bin is placed on the top of the crushing chamber. A collecting bin is placed underneath the crushing chamber. The two toothed rollers are placed horizontally facing each other and are fitted with 27 crushing teeth arranged in a staggered pattern. The comb teeth are staggered with the toothed roller to remove material stuck between the crushing teeth. The shattering beam is located between the toothed rollers and works in conjunction with the toothed rollers to control the size of the discharge material. The key dimensions of the TDRC are shown in Table 1.

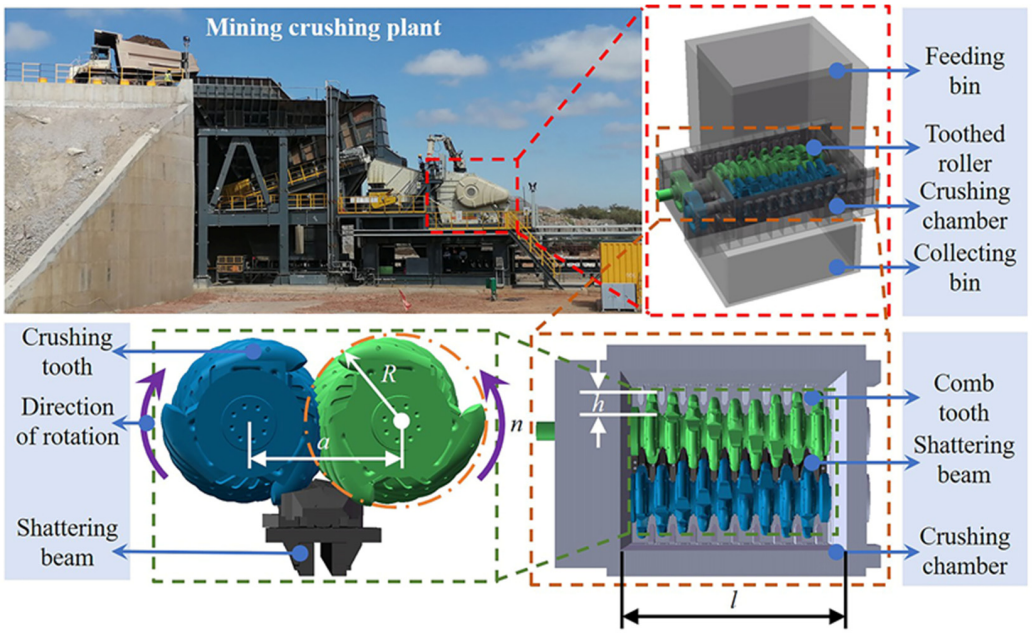


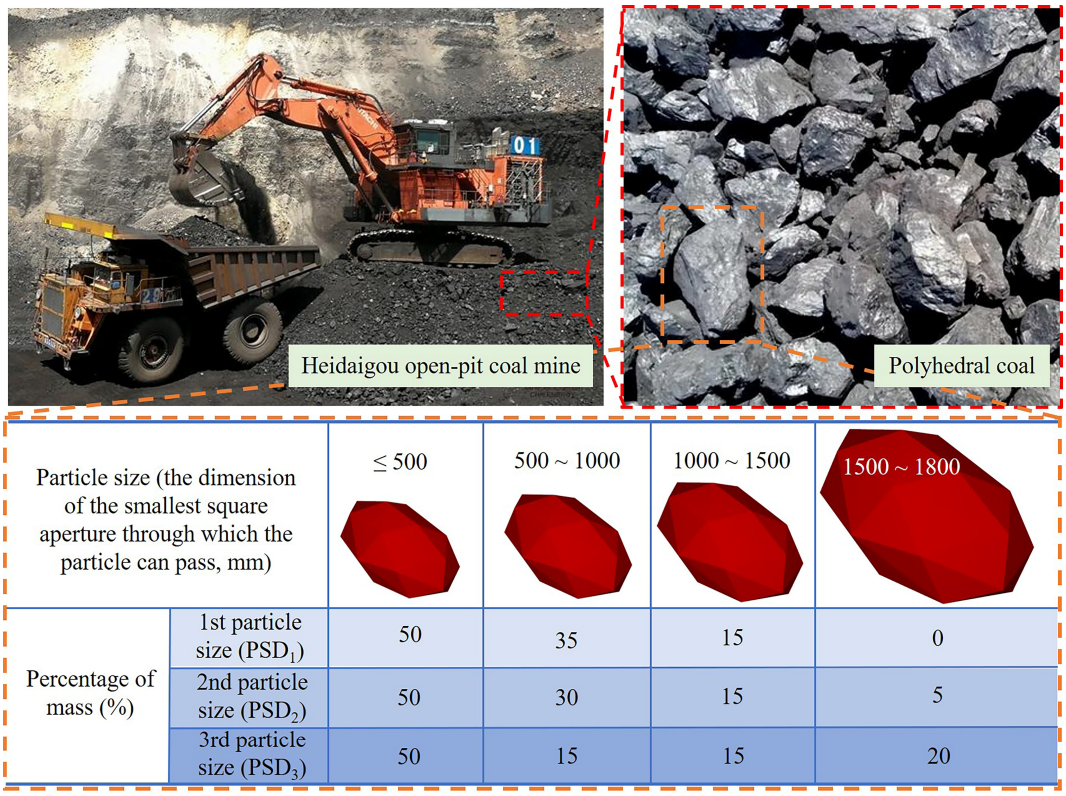
Figure 1. Toothed double-roll crusher.

Table 1. Key dimensions of the toothed double-roll crusher.

Parameter	Toothed Roller Shaft Distance/*a*	Toothed Roller Radius/*R*	Crushing Teeth Radial Height/*h*	Toothed Roller Length/*l*
Value (mm)	1000	548.5	312	2957

2.2. Actual Crushed Materials

The crushed objects in the Heidaigou open-pit coal mine are mainly polyhedral coal particles, as shown in Figure 2. There are three main size distributions of the feed particle: the 1st particle size, the 2nd particle size, and the 3rd particle size. The main difference between them is that the 1st particle size excludes large particles of 1500–1800 mm.



Particle size (the dimension of the smallest square aperture through which the particle can pass, mm)		≤ 500	500 ~ 1000	1000 ~ 1500	1500 ~ 1800
Percentage of mass (%)	1st particle size (PSD_1)	50	35	15	0
	2nd particle size (PSD_2)	50	30	15	5
	3rd particle size (PSD_3)	50	15	15	20

Figure 2. Coal particles and DEM model.

2.3. DEM Modelling of Crushed Materials

The DEM model of coal is built based on polyhedral configurations and corresponding real-size distributions, and each particle size and mass satisfy a semi-log plot as follows.

$$m = A + B \cdot \log(L) \quad (1)$$

where, A, B—fitting coefficients obtained on the basis of actual particle mass and size; m—particle mass; L—particle size.

In the DEM simulation process, to determine the kinematic behaviour of the particles at each moment, the normal contact force, tangential contact force, and rolling friction between elements (particle–particle, particle–boundary) need to be calculated. So the contact plane where the contact force is located needs to be determined first. For spherical particles, the determination of the contact force is relatively simple, and for non-spherical

particles, the determination of the contact force is relatively complex based on grid division and nearest neighbour search algorithm.

2.3.1. Normal Force

Normal contact force is obtained based on the normal contact model, a normal force model for a DEM simulation has two major requirements. First, the force has to be a repulsive one. Second, the normal contact force model has to allow significant energy dissipation since a granular medium is an extremely dissipative system. Considering that coal is a low water content and compressible material, the hysteretic linear spring model, first proposed by Walton et al. [27], is used to obtain the normal contact force; see Equation (2). This elastic-plastic (repulsive and dissipative) normal contact model allows simulation of the plastic energy dissipation on a contact without introducing the overhead of long simulation times. In addition, since no viscous damping term is used, the energy dissipation is not dependent on the relative velocities of neighbouring particles, making the energy dissipation insensitive to other contacts. An additional advantage of this model is that compressible materials can be accurately modelled because the contact forces can be almost zero even at residual overlaps.

A typical cycle of loading/unloading is depicted in Figure 3. A → B → C is the first loading cycle, and repeating the loading again is the secondary loading cycle. Long-term contact is the loading cycle of three times or more. Between points A and B, we have the loading process, in which the normal force overlap increases linearly. After reaching the maximum overlap, the unloading follows a steeper line between points B and C. The plastic deformation for the contact only exists during the contact, so any residual deformation is forgotten after the contact ceases. The energy dissipated in the collision is numerically equal to the shaded area in the force-deformation diagram of Figure 3.

$$F_n^t = \begin{cases} \min\left(K_{nl}s_n^t,\ F_n^{t-\Delta t} + K_{nu}\Delta s_n\right) \text{ if } \Delta s_n \geq 0 \\ \max\left(F_n^{t-\Delta t} + K_{nu}\Delta s_n,\ \lambda K_{nl}s_n^t\right) \text{ if } \Delta s_n \prec 0 \end{cases} \tag{2}$$

where, F_n^t—normal elastic-plastic contact forces at the current time t, $F_n^{t-\Delta t}$—normal elastic-plastic contact forces at the previous time $t - \Delta t$, Δt—timestep, Δs_n—change in the contact normal overlap during the current time (see Equation (3)). It is assumed to be positive as particles approach each other and negative when they separate. s_n^t—normal overlap values at the current time t, $s_n^{t-\Delta t}$—normal overlap values at the previous time $t - \Delta t$, K_{nl}—value of loading contact stiffnesses, same slope as line AB, see Equation (4), K_{nu}—value of unloading contact stiffnesses, same slope as line BC, see Equation (5), λ—dimensionless small constant (0.001), it is determined through a set of calibration tests. The part of the expression in which this constant is active ensures that, during the unloading, the normal force will return to zero when the overlap decreases to zero.

$$\Delta s_n = s_n^t - s_n^{t-\Delta t} \tag{3}$$

The loading and unloading stiffnesses are defined by the particle size, the bulk Young's modulus, and the restitution coefficient of contacting materials.

$$\frac{1}{K_{nl}} = \begin{cases} \frac{1}{K_{nl,p1}} + \frac{1}{K_{nl,p2}}, & \text{for particle} - \text{particle contact} \\ \frac{1}{K_{nl,p}} + \frac{1}{K_{nl,b}}, & \text{for particle} - \text{boundary contact} \end{cases} \tag{4}$$

where, $K_{nl,p}$—loading contact stiffnesses of particles, $K_{nl,b}$—loading contact stiffnesses of boundary.

$$K_{nu} = \frac{K_{nl}}{\varepsilon^2} \tag{5}$$

where, ε- restitution coefficient,$K_{nl,p}$ and $K_{nl,b}$ can be obtained by the following:

$$K_{nl,p} = E_p \cdot L \tag{6}$$

$$K_{nl,b} = E_b \cdot L \tag{7}$$

where, E_p—particle material's bulk Young's modulus or elastic modulus, E_b—boundary material's Young's modulus.

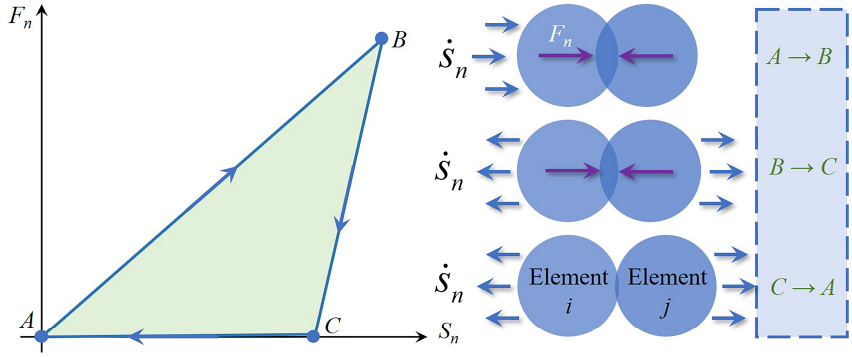


Figure 3. Schematic diagram of a typical loading and unloading cycle.

In long-term contacts, for instance, among particles in a stockpile, the hysteretic linear spring model can give rise to oscillations of very small amplitudes on the normal force and on the overlap. Although these oscillations are barely noticeable, this phenomenon can prevent the particles from reaching a state of absolute repose. Because of this, an additional mechanism of energy dissipation is introduced to dissipate spurious oscillations in long-term contacts. This mechanism consists of the addition of a viscous force, which is only activated during secondary loading cycles on long-term contacts. That additional force is defined in a similar fashion to that of the dissipative part of the contact force on the linear spring-dashpot model proposed by Cundall et al. [28]:

$$F_{n,v} = C_n \cdot \dot{s}_n \tag{8}$$

where, $\dot{s}_n$—normal overlap velocity, C_n—damping coefficient, can be obtained by following:

$$C_n = 2\eta\sqrt{m * K_{nl}} \tag{9}$$

where, η—damping ratio (0~1), whose value is related to the restitution coefficient [29], see below:

$$\varepsilon = \begin{cases} \exp\left[-\frac{\eta}{\sqrt{1-\eta^2}}\left(\pi - \arctan\frac{2\eta\sqrt{1-\eta^2}}{1-2\eta^2}\right)\right] & \text{if } 0 \le \eta \le \frac{1}{\sqrt{2}} \\ \exp\left[-\frac{\eta}{\sqrt{1-\eta^2}}\arctan\frac{2\eta\sqrt{1-\eta^2}}{2\eta^2-1}\right] & \text{if } \frac{1}{\sqrt{2}} \le \eta \le 1 \\ \exp\left[-\frac{\eta}{\sqrt{1-\eta^2}}\ln\frac{\eta+\sqrt{\eta^2-1}}{\eta-\sqrt{\eta^2-1}}\right] & \text{if } \eta \succ 1 \end{cases} \tag{10}$$

where, m*—effective mass for the contact, defined as:

$$\frac{1}{m*} = \begin{cases} \frac{1}{m_1} + \frac{1}{m_2} & \text{for particle} - \text{particle contact} \\ \frac{1}{m} & \text{for particle} - \text{boundary contact} \end{cases} \quad (11)$$

where, m_1, m_2—masses of the contacting particles, m—mass of the particle in contact with a boundary.

2.3.2. Tangential Force

The linear spring Coulomb limit model is used to calculate tangential force, where it is elastic fictional; its value at time t is given by:

$$F_{\tau,e}^{t} = F_{\tau}^{t-\Delta t} - K_{\tau}\Delta s_{\tau} \quad (12)$$

where, $F_{\tau}^{t-\Delta t}$—tangential force at the previous time, Δs_{τ}—tangential relative displacement of the particles during the timestep, and K_{τ}—tangential stiffness, defined as:

$$K_{\tau} = r_K \cdot K_{nl} \quad (13)$$

where, r_K—tangential stiffness ratio.

It is important to note that the tangential force cannot exceed the Coulomb limit; in other words, the sliding is considered to be taking place on the contact the first time the tangential force exceeds the Coulomb limit. Once that force falls below the value of the Coulomb limit, the contact is considered non-sliding again. Therefore, the complete expression for the tangential force is:

$$\mathbf{F}_{\tau}^{t} = \min\left(\left|\mathbf{F}_{\tau,e}^{t}\right|, \mu F_{n}^{t}\right) \frac{\mathbf{F}_{\tau,e}^{t}}{\left|\mathbf{F}_{\tau,e}^{t}\right|} \quad (14)$$

where, μ—friction coefficient, defined as:

$$\mu = \begin{cases} \mu_s \text{ if no sliding takes place at the contact} \\ \mu_d \text{ if sliding does take place at the contact} \end{cases} \quad (15)$$

where, μ_s—static friction coefficient, μ_d—dynamic friction coefficient.

2.3.3. Rolling Resistance

Rolling resistance is the common methodology used when a moment that opposes the rolling motion of a particle is introduced into the modelling; as a practical way, it can represent the effect of non-sphericity on rolling spheres or the effect of surface irregularities on other types of particles. In this paper, an elastic-plastic rolling model is used to obtain the rolling resistance [30]; it can be realised that the proper choice of the rolling stiffness value provides good behaviour of the rolling resistance without any additional damping [31], where the rolling stiffness is defined as:

$$K_r = R_r^2 K_{\tau} \quad (16)$$

where, R_r—rolling radius, given by:

$$\frac{1}{R_r} = \begin{cases} \frac{1}{r_1} + \frac{1}{r_2} & \text{for particle} - \text{particle contact} \\ \frac{1}{r} & \text{for particle} - \text{boundary contact} \end{cases} \quad (17)$$

where, r_1, r_2—rolling radii of the contacting particles, and r—rolling radius of the particle in contact with the boundary.

If the rolling resistance is purely elastic, the rolling resistance moment is updated incrementally in the following way:

$$\mathbf{M}_{r,e}^{t} = \mathbf{M}_{r}^{t-\Delta t} - K_r \boldsymbol{\omega}_{rel} \Delta t \tag{18}$$

where, $\mathbf{M}_{r}^{t-\Delta t}$—rolling resistance moment vector at the previous time, $\boldsymbol{\omega}_{rel}$—relative angular velocity vector.

Further, the magnitude of the rolling resistance moment is limited by the value that is achieved at a full mobilisation rolling angle. The limiting value [32] is:

$$M_{r,\mathrm{lim}} = \mu_r R_r F_n \tag{19}$$

where, μ_r—rolling resistance coefficient.

The final expression for the rolling resistance moment in the elastic-plastic rolling model:

$$\mathbf{M}_{r}^{t} = \min\left(\left|\mathbf{M}_{r,e}^{t}\right|, M_{r,\mathrm{lim}}\right) \frac{\mathbf{M}_{r,e}^{t}}{\left|\mathbf{M}_{r,e}^{t}\right|} \tag{20}$$

2.4. Crushing Force Calculation

The accurate acquisition of the crushing force is an important factor in the reproduction of the TDRC performance. Considering that there is a phenomenon of multiple cumulative crushings of ore particles during the TDRC crushing process, the Ab-T_{10} breakage model is used to achieve the crushing of the ore particles.

The Ab-T_{10} breakage model is based on the model posed by Vogel et al. [33] and the subsequent modification proposed by Shi et al. [34]. It treats every particle as a single entity that can be broken into fragments instantaneously based on the impact energy it receives. The total specific contact energy (e_c) is computed by summing the work carried out by the contact forces at all contact points in a particle during the loading period. To damage the particle, the total specific contact energy should be greater than the minimum breakage energy of the particle (e_{min}). This minimum breakage energy is related to the particle size, as follows:

$$e_{\mathrm{min}} = e_{\mathrm{min},ref} \frac{L_{ref}}{L} \tag{21}$$

where, $e_{\mathrm{min},ref}$—reference minimum specific energy value for a reference ore particle size, it can be obtained by calibration, as described in Section 3.1, L_{ref}—reference particle size, it can be obtained by the actual particle size distribution used in the crusher.

To take into account the damage caused by successive collisions, the granule breakage is made by considering a cumulative value of the specific contact energy (e_{cum}). If e_c^t is the instantaneous value of the specific contact energy at a given time t during a loading phase, the cumulative value of the specific contact energy will be updated only if $e_c^t > e_{cum}$ and $e_c^t > e_{\mathrm{max}}$ (the maximum value of contact energy registered on the particle until the last time in which the value of e_{cum} is updated). When those conditions are satisfied, the update is made according to the expression:

$$e_{cum}^{t} = e_{cum}^{t-\Delta t} + \left(e_c^t - e_c^{t-\Delta t}\right) \tag{22}$$

where, $e_{cum}^{t-\Delta t}$—cumulative specific contact energy at the previous timestep, $e_c^{t-\Delta t}$—specific contact energy at the previous timestep. Whenever the particle is unloaded and the value

of e_c^t decreases below $e_{\min}$, $e_{\max}$ is reset to zero, so a new cycle of loading may begin, in which the value of e_{cum} will be able to increase again.

The fracture probability function of a particle subjected to multiple impacts was shown to be:

$$P(e_{cum}) = 1 - \exp\left(-S \cdot e_{cum} \frac{L}{L_{ref}}\right) \tag{23}$$

where, S—selection function coefficient.

A particle will be broken if e_{cum} can be obtained by Equation (22) at any moment, and the fragments are generated following the Voronoi fracture algorithm [35,36] based on the particle size distribution. Here, corresponding size distributions can be generated based on the t_{10} value (the percentage of fragments passing a screen size of 1/10th of the original particle size L) and the Gaudin-Schumann distribution with a unitary slope:

$$\begin{cases} t_{10} = M\left(1 - \exp\left(-S \cdot e_{cum} \frac{L}{L_{ref}}\right)\right) \\ \gamma = 10 t_{10}\left(\frac{x}{L}\right) \end{cases} \tag{24}$$

where, M—maximum t_{10} for a material subject to breakage, γ—cumulative percentage of the mass of passing fragments, x—screening sieve size, and L—size of the broken particle.

New fragments created by fragmentation will be further fragmented if they are subjected to additional damage, creating smaller fragments.

3. Modelling and Validation of TDRC

3.1. Calibration and Setup of Parameters

Before the DEM simulation can be carried out, it is necessary to select appropriate material parameters of particle and boundary, contact parameters of particle-particle and particle-boundary, and particle crushing parameters. In this paper, the material parameters and contact parameters are set based on the existing database [37,38] and the parameters provided by the Heidaigou open-pit coal mine, as shown in Table 2.

Table 2. Material parameters and contact parameters used in DEM simulation.

Parameters	Symbol	Coal	
		5.5 MPa Coal	Boundary (Steel)
Density (kg/m^3)	ρ	2216.67	7850
Poisson's ratio	v	0.35	0.3
Young's modulus (Pa)	E	3.5×10^9	2.06×10^{11}
Restitution coefficient	ε	0.4	0.5
Static friction coefficient	μ_s	0.7	0.6
Dynamic friction coefficient	μ_d	0.06	0.05

Referring to the extant literature, crushing parameters are calibrated based on a trial-and-error method. That is, a set of crushing parameters with similar compressive strength is selected concerning the results of existing studies; on this basis, the desired compressive strength is achieved by adjusting the value of a single factor. In the Heidaigou open-pit coal mine, coal mainly consists of hard and soft coal, with corresponding compressive strengths of 16.8 MPa and 5.5 MPa, respectively. This section focuses on the coal crushing process through common uniaxial compression methods [18], as shown in Figure 4. During the compression process, setting the minimum crushing size as 50 mm, a receiving box is used to collect the generated coal particles to be crushed, and the platen is moved vertically downwards at a velocity (v_p) of 0.01 m/s until the coal particles are crushed. Here, the coal particle size is 0.5 m.

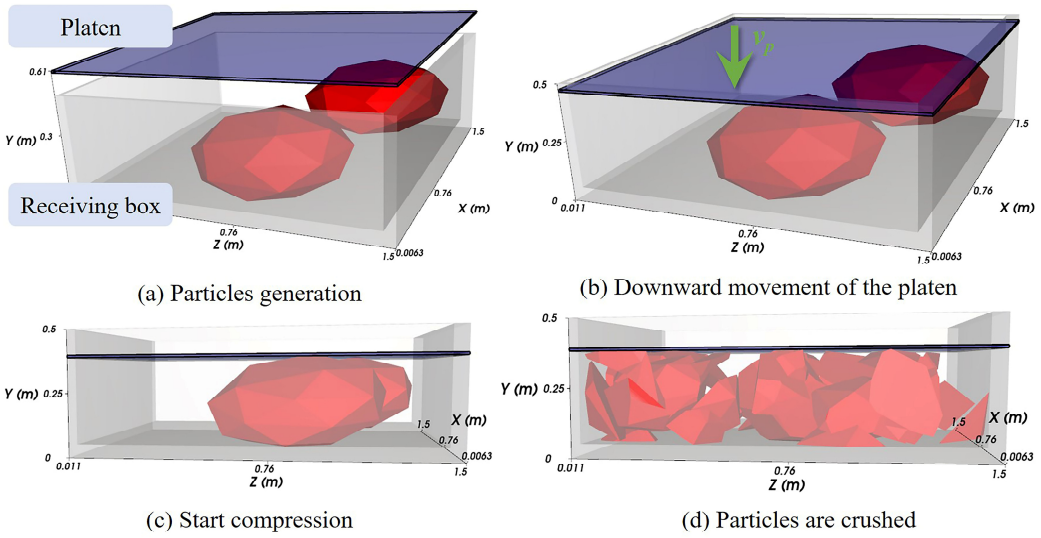


Figure 4. Schematic diagram of uniaxial compression test process.

The calibration procedure is to first calibrate the crushing parameters of 5.5 MPa coal based on Young's modulus of 3.5×10^9 Pa. Based on this, Young's modulus of 16.8 MPa coal is calibrated using the same crushing parameters. The corresponding calibration results are shown in Figure 5 and Table 3; it can be seen that Young's modulus of 16.8 MPa coal is 2×10^{10} Pa.

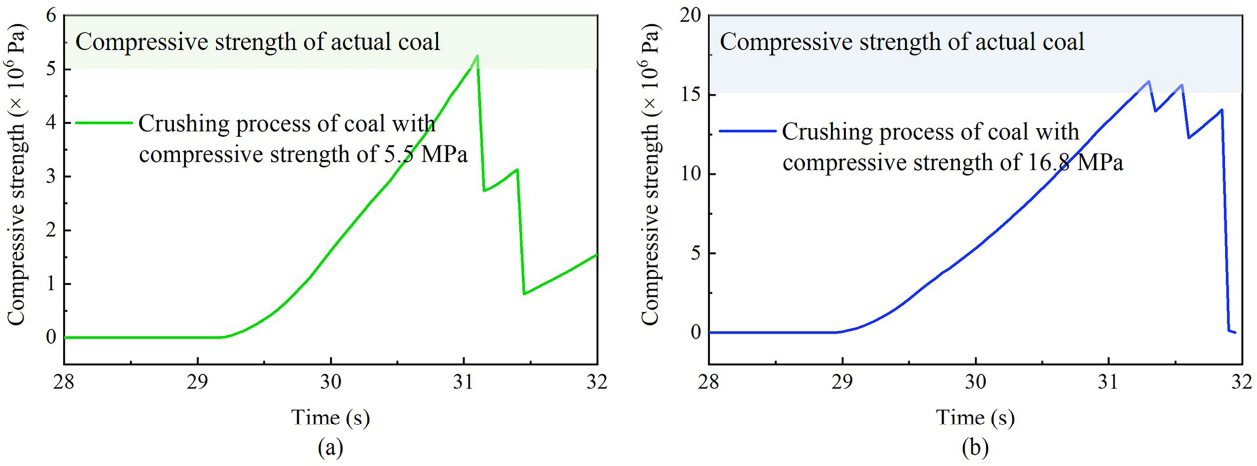


Figure 5. Calibration process of the crushing parameters. (**a**) Calibration process of 5.5 MPa coal, (**b**) Calibration process of 16.8 MPa coal.

Table 3. Calibration results of the crushing parameters.

Crushing Parameters	Coal	
	Soft	**Hard**
Reference size (mm)	50	50
Minimum crushing energy (J/kg)	1×10^9	1×10^9
Selection function coefficient (kg/J)	1000	1000
Maximum T_{10} (%)	67.71	67.71
Young's modulus (Pa)	3.5×10^9	2×10^{10}

3.2. DEM-MBD Model of TDRC

Considering that TDRC is a typical multi-body system, a simulation model of TDRC is constructed based on the multi-body dynamics (MBD) method according to the actual

geometric structure of TDRC as described in Section 2.1, which includes a feeding bin, collecting bin, scattering beam, toothed roller, crushing chamber, etc. Here, the crushing chamber is fixedly connected to the frame, and the feeding bin is fixed above the crushing chamber, the collecting bin is located below the crushing chamber. The toothed roller is located inside the crushing chamber; it is driven by a power source to produce face-to-face rotation. The scattering beam is located directly below the toothed roller and is fixed to the crushing chamber.

On this basis, to reproduce the working process of TDRC, the DEM-MBD coupling simulation model of TDRC is formed by integrating the DEM numerical simulation model of coal established in Section 2.2 and a DEM-MBD coupling interface for data exchange for Ansys Rocky® and Ansys Motion® (Southpointe 2600 Ansys Drive, Canonsburg, PA, USA). During a simulation process of DEM-MBD, the DEM model and the MBD model are simulated in an alternating manner, as shown in Figure 6. It is common that multiple time steps are required to simulate the same time period as a single time step of MBD simulation, so the time steps between the two models are potentially different. Here, taking into account the actual computing power of the computer in the laboratory (DELL T3660 (Dell Inc., Londrak, TX, USA), I9-13900K (5.8 GHz 24 cores), Memory: 64 GB DDR5), the time-steps of DEM and MBD are set to 1×10^{-5} s and 0.01 s, respectively, the simulation stable operation time not less than 5 s. Computer with 8–12 h of actual computing time per set of simulations.

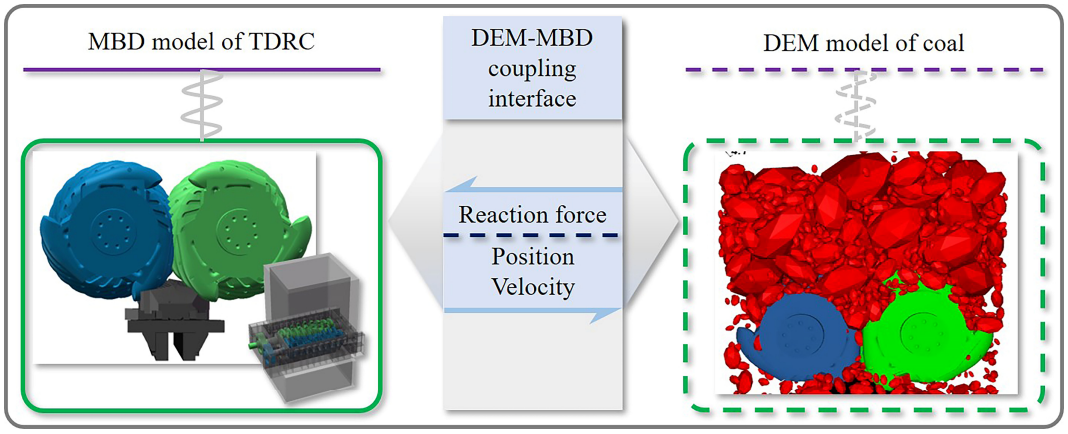


Figure 6. DEM-MBD coupling simulation model of TDRC.

3.3. Validation

In order to verify the effectiveness of the DEM-MBD coupling simulation model, the corresponding DEM-MBD coupling simulation is carried out based on the typical crushing conditions of the coal mine [39] in this section. Here, the height of the coals in the feeding bin is kept near 1.5 m, the rotation speed of the toothed roller is 33.3 r/min, and the size distributions of the feed particles are the 2nd particle size and the 3rd particle size with corresponding compressive strengths of 5.5 MPa and 16.8 MPa. The corresponding simulation process is shown in Figure 7a–c, and the results are listed in Table 4. Here, the power is obtained by Equation (25), the productivity is obtained by the curve of the mass of the discharged material over time, and the discharge granularity is obtained by counting the mass percentage of the discharged material.

$$P = T \cdot n/9550 \tag{25}$$

where, T—torque of toothed roller, is calculated as the average during the steady state phase of the operation, n—rotation speed of toothed roller.

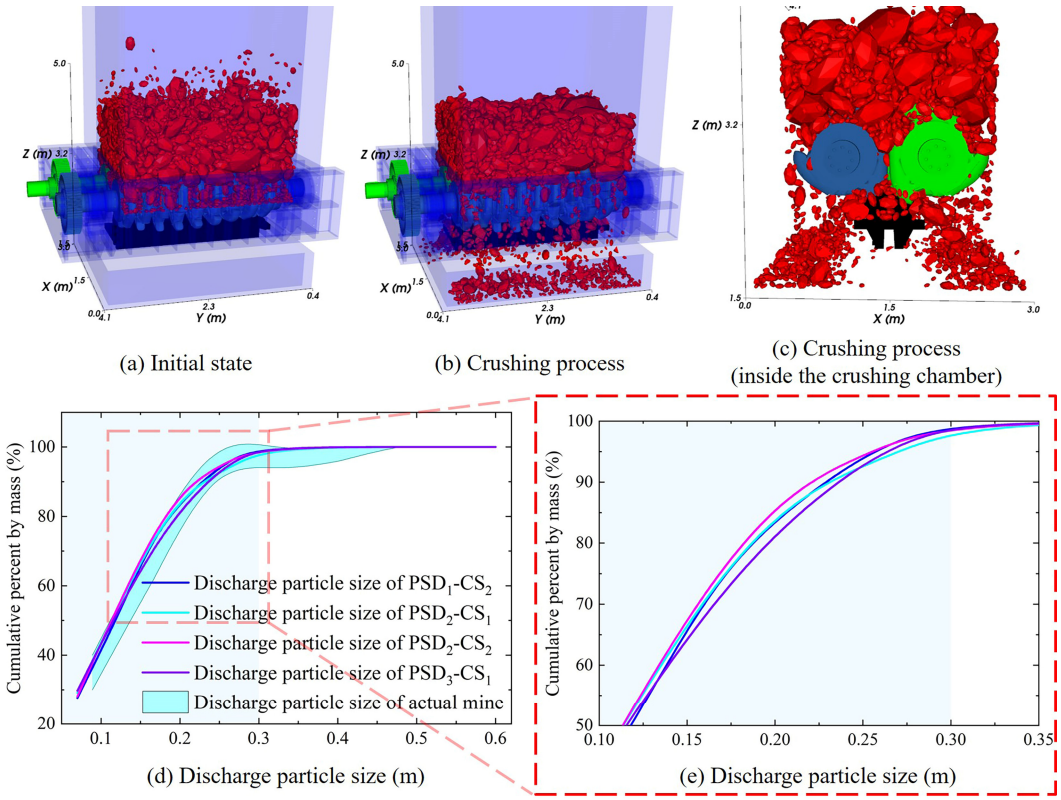


Figure 7. Validation simulation analysis of TDRC. The light blue area in the figure shows the discharge particle size within 0.3 m.

Table 4. Simulation results of typical crushing conditions.

TDRC Working Condition		Actual Value			DEM-MBD Coupling Simulation		
		Power (kW)	Productivity (t/h)	Discharge Granularity (≤300 mm, %)	Power (kW)	Productivity (t/h)	Discharge Granularity (≤300 mm, %)
Rotation speed of toothed roller (33.3 r/min)	PSD_2/CS_1	200~230	4000~5500	≥ 95	218.73	4896.61	97.75
	PSD_3/CS_1	280~315			290.33	5055.62	100
Rotation speed of toothed roller (33.3 r/min)	PSD_2/CS_2	240~273			250.57	4702.68	95.66
	PSD_3/CS_2	300~350			301.37	5158.37	98.78

It can be seen that the simulation results of the key indicators (power, productivity) are located within the distribution of the actual values in the mine. Further, the discharge particle size matches the actual one, as shown in Figure 7d,e. PSD_2, PSD_2, and PSD_3 represent the 1st particle size, 2nd particle size, and 3rd particle size, respectively. CS_1 represents a compressive strength of 5.5 MPa, and CS_2 represents a compressive strength of 16.8 MPa. The green banded lines in the figure indicate the corresponding discharge particle size of the actual mine, which initially verifies the effectiveness of the DEM-MBD coupling simulation model of TDRC.

4. Results and Discussion

4.1. DEM-MBD Test Scheme

To investigate the effects of particle size on the crushing performance of TDRC, the DEM-MBD coupling simulation in this paper is divided into two parts: small-particle simulation and large-particle simulation. The small particle simulation is based on the 1st particle size, and the large particle simulation is based on the 2nd particle size and 3rd particle size, and the test scheme is a comprehensive test. The impact factors are particle

size distribution, rotation speed of the toothed roller, and compressive strength of coal; the range of influence factors is determined based on the actual working conditions of the coal mine; see Table 5. The performance indexes include productivity (P), power (p), torque of toothed roller (T), and stress of toothed roller (maximum, σ). In addition, to characterise the output per unit of power consumption of TDRC, the power density (PD) is introduced, and it is calculated as follows:

$$PD = P/p \quad (26)$$

Table 5. Range of variation of impact factors.

Influence Factor	Particle Size Distribution (PSD)	Rotation Speed of Toothed Roller (RSTR, r/min)	Compressive Strength (CS, MPa)
Value	PSD_1 PSD_2 PSD_3	25 ($RSTR_1$) 33.3 ($RSTR_2$) 42 ($RSTR_3$)	CS_1 CS_2

4.2. Analysis of Small Particle Crushing Conditions

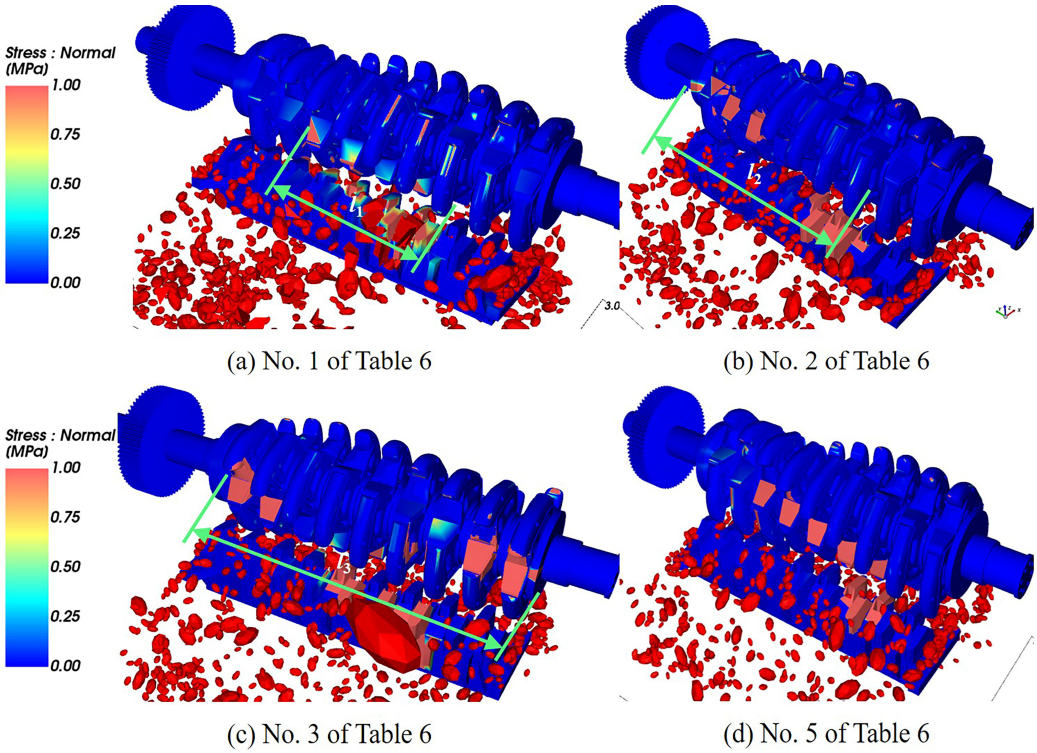
The results of small particle crushing are listed in Table 6. By means of the extreme variance analysis method, it can be seen that with the increase in the rotation speed of the toothed roller, the productivity and stress of the toothed roller increase rapidly and then increase less rapidly; the torque of the toothed roller takes the lead in increasing and then decreasing; and power is first increased and then stabilised (Table 7). This shows that the rotation speed of the toothed roller is the main influence factor on the crushing performance of TDRC when it works at low speed (25~33.3 r/min), and the rotation speed of the toothed roller is not the main influence factor on the power when TDRC works at high speed (33.3~42 r/min). The reason is that when the TDRC is working at low speed, the increase in rotation speed of the toothed roller can accelerate the coal particles into the effective crushing area formed by the crushing teeth engaging with each other and realise the rapid crushing of coal, which increases productivity. Secondly, the effective contact length between the toothed roller and coal particles is greatly increased; the effective contact length at 42 r/min covers the entire axial length of the toothed roller. As shown in Figure 8a–c, $l_1 < l_2 < l_3$, the stress of the toothed roller increases, which is also the reason for the change of torque of the toothed roller. In addition, the power density decreases and then stabilises under the low compressive strength of coal, and the power density tends to stabilise overall as the compressive strength increases, suggesting that the output per unit of power consumption is essentially stable, which is strongly correlated with the patterns of productivity change.

Table 6. Simulation results of small-particle crushing conditions.

No.	Impact Factor			Performance Index				
	PSD	CS	RSTR	P (t/h)	T (N·m)	p (kW)	PD (t/h/kW)	σ (MPa)
1	PSD_1	CS_1	$RSTR_1$	3647.50	28,915.49	151.39	24.09	99.36
2	PSD_1	CS_1	$RSTR_2$	4269.33	45,028.39	314.02	13.60	316.87
3	PSD_1	CS_1	$RSTR_3$	4421.91	30,275.77	266.30	16.60	351.63
4	PSD_1	CS_2	$RSTR_1$	3148.71	49,421.25	258.75	12.17	160.38
5	PSD_1	CS_2	$RSTR_2$	3754.44	43,369.33	302.45	12.41	335.53
6	PSD_1	CS_2	$RSTR_3$	4481.89	44,442.74	390.91	11.47	421.98

Table 7. Results of extreme variance analysis of small-particle crushing conditions.

No.	Impact Factor	Performance index				
		P (t/h)	T (N·m)	p (kW)	PD (t/h/kW)	σ (MPa)
1	CS_1	4112.91	34,739.88	243.90	18.10	255.95
2	CS_2	3795.01	45,744.44	317.37	12.02	305.96
3	$RSTR_1$	3398.11	39,168.37	205.07	18.13	129.87
4	$RSTR_2$	4011.89	44,198.86	308.24	13.01	326.20
5	$RSTR_3$	4451.90	37,359.26	328.61	14.03	386.81



(a) No. 1 of Table 6 (b) No. 2 of Table 6

(c) No. 3 of Table 6 (d) No. 5 of Table 6

Figure 8. Normal stress distribution of crushing teeth.

With the increase in compressive strength of coal, the productivity decreases, and this phenomenon disappears gradually at high speeds. Crushing hard coal requires higher crushing energy, thus requiring the TDRC to be crushed several times, which in turn reduces productivity. This also shows that the compressive strength of coal is the main determinant of productivity at low-speed conditions (25~33.3 r/min), and the rotation speed of the toothed roller is the main influencing factor of productivity at high-speed conditions (33.3~42 r/min). Secondly, the torque of the toothed roller, power, and stress of the toothed roller increase. The reason is that due to the increase in the compressive strength of coal, the contact time between crushing teeth and coal particles increases. In the case of the stress of the toothed roller, this situation is weakened by the increase in rotation speed of the toothed roller. The normal stress distributions of crushing teeth for No. 2 of Table 6 and No. 5 of Table 6 are essentially the same as shown in Figure 8b,d. This indicates that the high-speed operation (33.3~42 r/min) can effectively disturb the coal particles in the crushing chamber, and the contact effect between the coal particles can accelerate the crushing of coal particles, which in turn relieves the stress of the toothed roller.

4.3. Analysis of Large Particle Crushing Conditions

The results of large particle crushing are listed in Table 8. By means of extreme variance analysis method, it can be seen that with the increase in rotation speed of toothed roller and

compressive strength of coal, the performance indexes include productivity, power, torque of toothed roller, and stress of toothed roller follow a similar evolutionary pattern to that of Section 4.2. It is important to note that all performance indicators increase rapidly and then increase less rapidly as the mass percentage of large-size coal particles (1500–1800 mm) increases, which indicates that a certain amount of large-size coal particles (mass percentage of 5–20%) can improve productivity to a certain extent, but it is also accompanied by an increase in power consumption. This is because, although large particles are easy to prolong the crushing time, at this time the large particles are relatively easy to break down, and a high mass percentage of the small-sized particles of the broken particles are easily discharged from TDRC. In addition, the presence of large particles causes the small particles to come into reliable contact with the toothed roller without up-arching, which in turn allows the small particles to be crushed further, thereby improving productivity. Further, the power density decreased by 5.89% as the mass percentage of large-sized coal particles increased, and this phenomenon is weakened with the increase in the compressive strength of coal, which is related to the increase in power consumption.

Table 8. Simulation results of large-particle crushing conditions.

No.	Impact Factor			Performance Index				
	PSD	CS	RSTR	P (t/h)	T (N·m)	p (kW)	PD (t/h/kW)	σ (MPa)
1	PSD_2	CS_1	$RSTR_1$	4149.40	35,247.14	184.54	22.49	242.69
2	PSD_2	CS_1	$RSTR_2$	4896.61	31,364.44	218.73	22.39	329.56
3	PSD_2	CS_1	$RSTR_3$	5542.85	31,777.63	279.51	19.83	528.78
4	PSD_2	CS_2	$RSTR_1$	4332.60	32,357.31	169.41	25.57	267.23
5	PSD_2	CS_2	$RSTR_2$	4702.68	35,930.08	250.57	18.77	224.59
6	PSD_2	CS_2	$RSTR_3$	5496.95	46,577.85	409.69	13.42	438.48
7	PSD_3	CS_1	$RSTR_1$	4326.01	37,978.44	198.84	21.76	254.72
8	PSD_3	CS_1	$RSTR_2$	5055.62	41,631.40	290.33	17.41	475.61
9	PSD_3	CS_1	$RSTR_3$	5846.62	30,575.92	268.94	21.74	440.60
10	PSD_3	CS_2	$RSTR_1$	4260.89	35,212.76	184.36	23.11	121.33
11	PSD_3	CS_2	$RSTR_2$	5158.37	43,214.47	301.37	17.12	217.86
12	PSD_3	CS_2	$RSTR_3$	5635.30	42,010.90	369.52	15.25	474.44

For Nos. 1, 4, and 7, 10 in Table 8, when the coal particle is the 2nd particle size, the productivity increases by 200 t/h as the compressive strength of coal increases. However, when the coal particle is 3rd particle size, the productivity decreases by about 60 t/h in the same case, which indicates that the compressive strength of coal is no longer the dominant factor for productivity when there are more large-sized particles. For Nos. 1~3 and 7~9 in Table 8, when the coal particle is 2nd particle size, the productivity increases by about 1400 t/h with the increase in rotation speed of the toothed roller, when the coal particle is 3rd particle size, the productivity increase by about 1500 t/h in the same case, which indicates that the rotation speed of toothed roller is the dominant factor for productivity when there are more large-sized particles (Increase in mass percentage by 15%). The main reason is that the high gravity of the large-sized particles makes the large-sized particles and the high-speed toothed roller form a reliable contact, coupled with high meshing force from the toothed roller at this time so that the coal particles are easy to break.

4.4. Analysis of Discharge Particle Size

As shown in Table 9. For the small-size crushing condition, the mass percentage of the discharge particle size lower than 300 mm is above 87%, and the mass percentage of the discharge particle size lower than 250 mm is above 78%. Secondly, with the increase in the rotation speed of the toothed roller, the mass percentage of the discharge particle

size lower than 300 mm decreases (decrease of approximately 13%), which indicates that the TDRC can achieve high productivity under the condition of high rotation speed of the toothed roller, but the quality of the discharged particle deteriorates, which also shows that there are more flaky coal particles that are not sufficiently crushed. In addition, with the increase in compressive strength, the quality of the discharge particle size increases.

Table 9. Discharge particle size of TDRC.

Test Condition	Test No.	Percentage of Mass (%)	
		≤300 mm	≤250 mm
Small particle crushing condition	1	96.81	89.25
	2	88.2	84.27
	3	87.88	78.47
	4	97.56	91.18
	5	89.97	84.34
	6	87.45	78.51
Large particle crushing condition	1	99.94	89.84
	2	97.75	89.62
	3	97.29	88.83
	4	96.36	91.1
	5	95.66	89.81
	6	97.79	90.19
	7	100	92.19
	8	97.52	91.38
	9	100	94.68
	10	98.78	92.76
	11	97.87	88.72
	12	97.69	87.72

For the large-size crushing condition, the mass percentage of particles with a discharge size lower than 300 mm is above 97%, and the mass percentage of particles with a size lower than 250 mm is above 87%, which is higher than that of the small-size crushing condition. It also indicates that an appropriate increase in the large size of the coal particles can improve the crushing quality of the TDRC, which is in line with the conclusions in Section 4.3. In addition, with the increase in compressive strength, discharge particle size quality decreases, which is different from the small particle crushing conditions. The reason is related to the presence of large-size particles of 1500–1800 mm.

The discharged particle size under 33.3 r/min crushing condition is shown in Figure 9a; it can be seen that the discharged particle quality of the small particle crushing condition (PSD_1-CS_1, PSD_1-CS_2) is lower than that of the large particle crushing condition (approximately 10% with a discharge size lower than 300 mm), which is consistent with the results of the above analyses. Secondly, the discharge particle quality at a particle size lower than 200 mm of a small particle crushing condition is better than that of a large particle crushing condition (Figure 9b), which may be related to the high mass percentage of particles with a size of 500~1000 mm; the size of these coal particles after being crushed is mainly distributed below 200 mm.

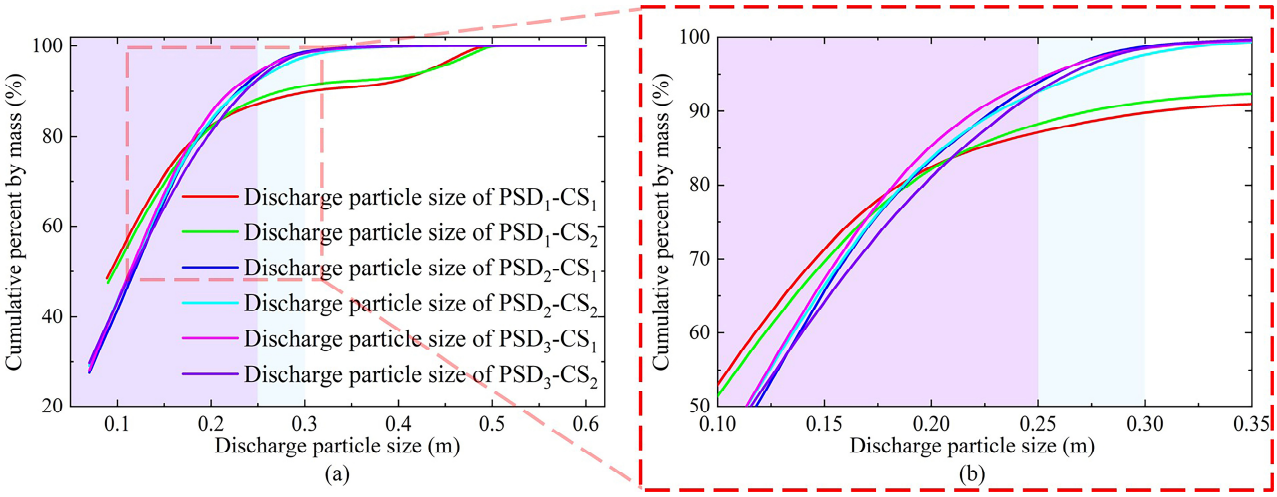


Figure 9. Discharge particle size at 33.3 r/min crushing condition. (**a**) Full size discharge particle size distribution, (**b**) Discharge particle size distribution within 0.35 m.

5. Conclusions

The toothed double-roll crusher that is most widely used in the Heidaigou open-cast coal mine is taken as the research object in this paper. The coupled simulation model of the toothed double-roll crusher based on the DEM-MBD and Ab-T_{10} breakage model is constructed, and the crushing performance under different feed particle sizes, compressive strengths of coal, and rotation speeds of the toothed roller is analysed by integrating comprehensive tests. The main conclusions of this study are as follows:

1. The rotation speed of the toothed roller is the main influence factor on the crushing performance of the toothed double-roll crusher when it works at 25~33.3 r/min, and it is not the main influence factor on the power consumption when it works at 33.3~42 r/min.
2. With the increase in compressive strength of coal, the productivity decreases, and this phenomenon disappears gradually at high-speed conditions. Meanwhile, the coal particles in the crushing chamber can be effectively perturbed, and the contact effect between them can accelerate their breakage, which in turn relieves the stress of the toothed roller.
3. A certain amount of large-size coal particles can improve productivity to a certain extent, but it also comes with an approximately 16–23% increase in power consumption, and the rotation speed of the toothed roller is the dominant factor for productivity when there are more large-sized particles.
4. The toothed double-roll crusher can achieve high productivity under high-speed conditions, but the quality of the discharged material deteriorates, and a 5–20% increase in the large size of the coal particles can improve the crushing quality of the toothed double-roll crusher.
5. The power density decreased by 5.89% as the mass percentage of large-size coal particles increased, and this phenomenon is weakened with the increase in the compressive strength of coal.

Author Contributions: Conceptualization, Z.C. and D.X.; methodology, Z.C. and G.W.; software, Z.L. (Zhengbin Liu); validation, Z.C., Z.L. (Zhengjie Lei), and Z.L. (Zhengbin Liu); formal analysis, Z.C.; investigation, Z.C.; writing—original draft preparation, Z.C. and D.X.; writing—review and editing, Z.C. and D.X.; supervision, G.W.; funding acquisition, Z.C. and D.X. All authors have read and agreed to the published version of the manuscript.

Funding: This research was financially supported by the National Natural Science Foundation of China, grant number 52305275; the Fundamental Research Program of Shanxi Province, grant numbers TZLH20230818004, 202303021212072, and 202303021222180; the Shanxi Provincial Higher Education Science and Technology Innovation Project, grant number 2023L183; and the Open Project of the State Key Laboratory of Engine and Powertrain System, grant number skleps-sq-2023-015.

Data Availability Statement: The original contributions presented in this study are included in the article. Further inquiries can be directed to the corresponding authors.

Conflicts of Interest: Author Zhengjie Lei was employed by Taiyuan Heavy Industry Co., Ltd. The remaining authors declare that the research was conducted in the absence of any commercial or financial relationships that could be construed as a potential conflict of interest.

References

1. Cui, D.; Wang, G.; Lu, Y.; Sun, K. Reliability design and optimization of the planetary gear by a GA based on the DEM and Kriging model. *Reliab. Eng. Syst. Saf.* **2020**, *203*, 107074. [CrossRef]
2. Cleary, P.W.; Sinnott, M.D. Simulation of particle flows and breakage in crushers using DEM: Part 1—Compression crushers. *Miner. Eng.* **2015**, *74*, 178–197. [CrossRef]
3. Chen, Z.; Wang, G.; Xue, D.; Cui, D. Simulation and optimization of crushing chamber of gyratory crusher based on the DEM and GA. *Powder Technol.* **2021**, *384*, 36–50. [CrossRef]
4. Chen, Z.; Wang, G.; Xue, D.; Bi, Q. Simulation and optimization of gyratory crusher performance based on the discrete element method. *Powder Technol.* **2020**, *376*, 93–103. [CrossRef]
5. Johansson, M.; Bengtsson, M.; Evertsson, M.; Hulthén, E. A fundamental model of an industrial-scale jaw crusher. *Miner. Eng.* **2017**, *105*, 69–78. [CrossRef]
6. Sinnott, M.D.; Cleary, P.W. Simulation of particle flows and breakage in crushers using DEM: Part 2—Impact crushers. *Miner. Eng.* **2015**, *74*, 163–177. [CrossRef]
7. Li, G.; Roufail, R.; Klein, B.; Nordell, L.; Kumar, A.; Sun, C.; Kou, J. Experimental evaluation of the conjugate anvil hammer mill—Comparison of semi-confined to confined particle breakage. *Miner. Eng.* **2019**, *137*, 34–42. [CrossRef]
8. Ghasemi Ardi, E.; Dong, K.J.; Yu, A.B.; Yang, R.Y. A combined experimental and DEM approach to determine the breakage of particles in an impact mill. *Powder Technol.* **2017**, *318*, 543–548. [CrossRef]
9. Wang, B.; Wang, G.; Wang, H.; Ding, Y.; Chen, T. Comparison of breakage behavior between the sieving crusher and ordinary teeth roll crushers. *Energy Sources Part A* **2019**, *41*, 252–259. [CrossRef]
10. Vasilyeva, N.; Golyshevskaia, U.; Sniatkova, A. Modeling and improving the efficiency of crushing equipment. *Symmetry* **2023**, *15*, 1343. [CrossRef]
11. Lindqvist, M.; Evertsson, C.M. Improved flow- and pressure model for cone crushers. *Miner. Eng.* **2004**, *17*, 1217–1225. [CrossRef]
12. Huang, D.; Fan, X.; Wu, D.; Yao, F. Multi-objective planning of cone crusher chamber, output and size reduction. *Miner. Eng.* **2007**, *20*, 163–172. [CrossRef]
13. Wu, S.; Wang, S.; Wang, G.; Fan, L.; Guo, J.; Liu, Z.; Zhang, H.; Guan, W.; Wang, Y.; Wu, Y. Study on productivity of eccentric roll crusher based on theory and experiment. *Miner. Eng.* **2024**, *206*, 108500. [CrossRef]
14. Wu, F.; Ma, L.; Zhao, G.; Wang, Z. Chamber optimization for comprehensive improvement of cone crusher productivity and product quality. *Math. Probl. Eng.* **2021**, *2021*, 5516813. [CrossRef]
15. Evertsson, C.M. Cone Crusher Performance. Ph.D. Thesis, Chalmers Tekniska Hogskola, Göteborg, Sweden, 2000.
16. Weerasekara, N.S.; Powell, M.S.; Cleary, P.W.; Tavares, L.M.; Evertsson, M.; Morrison, R.D.; Quist, J.; Carvalho, R.M. The contribution of DEM to the science of comminution. *Powder Technol.* **2013**, *248*, 3–24. [CrossRef]
17. Metzger, M.J.; Glasser, B.J. Simulation of the breakage of bonded agglomerates in a ball mill. *Powder Technol.* **2013**, *237*, 286–302. [CrossRef]
18. Chen, Z.; Wang, G.; Xue, D. An approach to calibration of BPM bonding parameters for iron ore. *Powder Technol.* **2021**, *381*, 245–254. [CrossRef]
19. Metzger, M.J.; Glasser, B.J. Numerical investigation of the breakage of bonded agglomerates during impact. *Powder Technol.* **2012**, *217*, 304–314. [CrossRef]
20. Yang, L.; Song, C.; Ai, L.; Liu, F.; Li, C.; Zhu, D.; Guo, C. Collision characteristics and breakage evolution of particles in fluidizing processes. *Fuel Process. Technol.* **2023**, *243*, 107654. [CrossRef]
21. ESSS-Rocky. *Rocky User Manual*; Rocky DEM, Inc.: Rio de Janeiro, Brazil, 2021.
22. Jiang, C.; Gou, D.; Li, C.; Wu, G.; An, X.; Wang, J.; Guo, P. Crushing characteristics and performance evaluation of iron ore in a cone crusher: A numerical study. *Miner. Eng.* **2023**, *204*, 108429. [CrossRef]

23. Quist, J.; Evertsson, C.M. Cone crusher modelling and simulation using DEM. *Miner. Eng.* **2016**, *85*, 92–105. [CrossRef]
24. Li, Y.W.; Zhao, L.L.; Hu, E.Y.; Yang, K.K.; He, J.F.; Jiang, H.S.; Hou, Q.F. Laboratory-scale validation of a DEM model of a toothed double-roll crusher and numerical studies. *Powder Technol.* **2019**, *356*, 60–72. [CrossRef]
25. Chen, G.; Wang, Q.; Xu, D.; Li, H.; He, J.; Lu, C. Design and experimental research on the counter roll differential speed solid organic fertilizer crusher based on DEM. *Comput. Electron. Agric.* **2023**, *207*, 107748. [CrossRef]
26. Liu, F.; Ai, L.; Xuan, G.; Shang, K.; Liu, Q.; Yang, L. Numerical study on collision and breakage characteristics of oxygen carrier particles in cold state in chemical looping combustion. *Powder Technol.* **2022**, *397*, 117023. [CrossRef]
27. Walton, O.R.; Braun, R.L. Viscosity, granular-temperature, and stress calculations for shearing assemblies of inelastic, frictional disks. *J. Rheol.* **1986**, *30*, 949–980. [CrossRef]
28. Cundall, P.A.; Strack, D.L. A discrete numerical model for granular assemblies. *Geotechnique* **1979**, *29*, 47–65. [CrossRef]
29. Schwager, T.; Poeschel, T. Coefficient of restitution and linear dashpot model revisited. *Granul. Matter* **2007**, *9*, 465–469. [CrossRef]
30. Ai, J.; Chen, J.F.; Rotter, J.M.; Ooi, J.Y. Assessment of rolling resistance models in discrete element simulations. *Powder Technol.* **2011**, *206*, 269–282. [CrossRef]
31. Wensrich, C.M.; Katterfeld, A. Rolling friction as a technique for modelling particle shape in DEM. *Powder Technol.* **2012**, *217*, 409–417. [CrossRef]
32. Derakhshani, S.M.; Schott, D.L.; Lodewijks, G. Micro–macro properties of quartz sand: Experimental investigation and DEM simulation. *Powder Technol.* **2015**, *269*, 127–138. [CrossRef]
33. Vogel, L.; Peukert, W. From single particle impact behaviour to modelling of impact mills. *Chem. Eng. Sci.* **2005**, *60*, 5164–5176. [CrossRef]
34. Shi, F.N.; Kojovic, T. Validation of a model for impact breakage incorporating particle size effect. *Int. J. Miner. Process.* **2007**, *82*, 156–163. [CrossRef]
35. Asahina, D.; Bolander, J.E. Voronoi-based discretizations for fracture analysis of particulate materials. *Powder Technol.* **2011**, *213*, 92–99. [CrossRef]
36. Gao, F.Q.; Stead, D. The application of a modified Voronoi logic to brittle fracture modelling at the laboratory and field scale. *Int. J. Rock Mech. Min.* **2014**, *68*, 1–14. [CrossRef]
37. Li, B.; Wang, Z.; Liang, C.; Wang, X. Modification of discrete element contact parameters of coal bulks based on rotary transport test. *J. Northeast. Univ.* **2021**, *42*, 1435–1443.
38. Liu, S.Y.; Jiang, H.X.; Gao, K.D. Simulation of coal mechanical characteristics with discrete element method. In Proceedings of the International Conference on Structures and Building Materials (ICSBM 2013), Guizhou, China, 9–10 March 2013; pp. 117–121.
39. Taiyuan Heavy Industry Co., Ltd. 2000–12000 T/H Double Toothed Roll Semi-Mobile Crushing Plant. 2023. Available online: http://www.tz.com.cn/cpzx1/kssb_/pshslsssb/a2000_12000t_hscgbydpsz.htm (accessed on 13 December 2023).

Disclaimer/Publisher's Note: The statements, opinions and data contained in all publications are solely those of the individual author(s) and contributor(s) and not of MDPI and/or the editor(s). MDPI and/or the editor(s) disclaim responsibility for any injury to people or property resulting from any ideas, methods, instructions or products referred to in the content.